Effect of interfacial vibrational coupling on surface wettability and water transport

Yechan Noh and N. R. Aluru

Effect of Interfacial Vibrational Coupling on Surface Wettability and Water Transport

Yechan Noh[1] and N. R. Aluru[2]

[1]Department of Mechanical Science and Engineering, University of Illinois at Urbana-Champaign, Urbana, Illinois 61801, United States

[2]Walker Department of Mechanical Engineering, Oden Institute for Computational Engineering and Sciences, The University of Texas at Austin, Austin 78712, United States

[2]*Correspondence should be addressed to aluru@utexas.edu*

KEYWORDS

Interfacial vibrational coupling, solid-liquid interfaces, dynamics, wettability, fluid slip, friction coefficient, molecular dynamics, water transport.

ABSTRACT

We report that the atomic-scale vibrational coupling at the solid-fluid interface can substantially alter the interfacial properties such as wettability and fluid slip. The wettability of water droplets on substrates subjected to various vibrational frequencies is studied using Molecular Dynamics (MD) simulation. The contact angle increases (*i.e.,* becomes more hydrophobic) when the oscillation frequency of the substrate matches the intermolecular bending frequency of liquid water. We investigate the underlying mechanism by examining the dynamics of water molecules at the interface and found that the temporal contact between the solid and fluid is shorter when the frequencies match, resulting in weak solid-fluid adsorption. We further report that the vibrational match at the interface reduces wall-fluid friction and enhances water transport through the nanopore. Our findings demonstrate the importance of the atomic-scale vibrational coupling at the solid-fluid interface on the physicochemical behavior of nanodevices and biological nanochannels.

INTRODUCTION

Thermal vibrations at a solid-fluid interface involve coupling between two fundamentally different mechanisms. The thermal fluctuations in a solid transfer energy without mass transport while the thermal motion of a fluid transfers both energy and mass. The vibrational coupling between them, referred to as interfacial vibrational coupling, creates a unique physical behavior and plays an important role in nanoscale transport phenomena. For example, Bernèche *et al.* [1] reported that the thermal fluctuations in biological channels considerably affect the ion selectivity by altering the free energy profile of the channel. Allen *et al.* [2] reported that the transport barriers of narrow pores are highly dependent on the instantaneous pore structure and emphasized the importance of thermal fluctuations of nanopores in ion permeation. A computational study performed by Ma *et al.* [3] reported that coupling between the water molecules and phonons of a carbon nanotube (CNT) causes oscillatory friction and enhanced water diffusion in the CNT. Marbach *et al.* [4] theoretically showed that a fluctuating surface changes the dispersion of nearby fluids, depending on the vibrational spectrum of a surface. While these prior studies emphasize the importance of fluctuations, there is, however, currently a lack of detailed understanding on how the solid-fluid vibrational coupling affects interfacial phenomena such as wetting, fluid slip and transport.

Wetting is an interfacial phenomenon related to numerous physicochemical problems. Surfaces with weak wetting (a hydrophobic surface for water) find applications in self-cleaning [5], anti-icing [6], and drag reduction [7]. Surfaces with strong wetting (a hydrophilic surface for water) are desirable for applications that require strong solid-fluid adhesion such as super-durable coating [8] and additive manufacturing [9]. The wettability of a surface can be characterized by the contact angle θ, which is determined by the balance between the liquid

3

cohesion forces and solid-liquid adhesion forces. Numerous methods have been investigated to engineer the wettability of a surface including nanostructuring [10], creating heterogeneous surfaces [11], graphene-coating [12], electric field [13], temperature [14], and vibration of a surface [15]. Li et al. [15] performed MD simulation of an aluminum droplet on a vibrating substrate. They observed that the wetting state changes from wetting to de-wetting at around $\omega = 6.7$ cm^{-1}, demonstrating the modulation of wetting using surface vibrations. However, the tested frequency range, $\omega = 3.3 \sim 33$ cm^{-1}, is narrow compared to the typical frequency range of thermal fluctuations ($\omega \lesssim 1\,000$ cm^{-1}). Werder *et al.* [16] presented that the flexibility of graphite has a negligible effect on the contact angle. On the contrary, Barisik and Beskok [17] reported that the thermal fluctuations of a silicon surface can change the contact angle of a water droplet and emphasized that thermal fluctuations should be properly considered for accurate estimation of the wetting behavior of silicon. Considering these studies, it is important to understand how the fluctuations of a surface affect the wetting behavior in a broad range of vibrational frequencies.

The fluid slip (non-zero fluid velocity) at a solid surface is one of the most distinctive phenomena in nanoscale fluidic transport. Due to the slip, the water flow in a small diameter CNT is several orders of magnitude faster compared to the prediction of classical fluid dynamics with no-slip assumption [18,19]. As the fluid slip can dominate fluid transport at molecular scale, slip must be properly considered in nanoscale fluidic phenomena [18–23]. There have been extensive studies on the physical parameters affecting slip such as surface roughness [24–27], curvature [21], surface charge [20], nanopore thickness [28], oxidation of surface [22], shear rate [29], solid-fluid interatomic force [29], and wettability [25,30,31]. There have also been reports on slip on a vibrating surface. Huang *et al.* [32] investigated fluid slip under imposed

4

shear-wave for a frequency range of $0.1 \text{ cm}^{-1} < \omega < 2.2 \text{ cm}^{-1}$ and found that slip is a frequency-dependent phenomenon. Computational studies reported slip enhancements in flexible CNT [33] and graphene nanochannels [34] compared to their rigid counterparts. Cao *et al.* [35] studied how phonon-modes of CNT affect the transport of water in a CNT membrane and reported highly enhanced water flux around the frequency of 33 cm^{-1}. Despite these early works, the molecular mechanisms at play in the interfacial vibrational coupling over a wide range of frequencies remains unclear.

In this study, we investigate the effect of interfacial vibrational coupling on wetting, fluid slip (wall-fluid friction), and fluid flow over a wide range of oscillation frequencies, $1 \text{ cm}^{-1} \leq \omega \leq 1\,000 \text{ cm}^{-1}$. We discuss the frequency range where the vibrational coupling affects the properties of the solid-fluid interface (*i.e.,* wettability and friction coefficient) and the molecular-level mechanisms. Then, we discuss the effect of interfacial vibrational coupling on the fluid slip in nanochannel and water transport through a nanopore.

RESULTS AND DISCUSSION

To study the effect of interfacial vibrational coupling on wetting behavior, we first considered a water droplet on the substrate (see Fig. 1(b)) that is oscillating in the out-of-plane direction where the vibrational energy corresponds to the thermal energy (see the Methods section for details). We then investigated how the frequency of the substrate affects the contact angle of the water droplet. Fig. 1(a) shows the various shapes of water droplets (visualized by the density) for different oscillation frequencies of the substrate, ω_s. In the rigid graphene, where the substrate does not oscillate (no interfacial vibrational coupling), the contact angle is obtained to be 43°, which is in good agreement with 42.4° reported in an earlier study by using the same forcefield [36]. The contact angle of a nanodroplet is subjected to size effect and the computed contact angle with 2 000 water molecules is slightly larger than the macroscopic contact angle of 38° obtained from extrapolation [16,36]. As our main objective is to study the interfacial vibrational coupling effect on wetting, we will use around this number of water molecules, which is most widely studied in previous contact angle calculations using MD simulations [11,16,36,37] for computational affordability. For all the vibrating substrates tested, we obtained higher contact angles (*i.e.,* hydrophobicity increases) compared to the contact angle on the rigid substrate. Fig. 1(c) shows the contact angle of a droplet as a function of the frequency of substrate. The maximum contact angle ($\theta = 117°$) is observed when the frequency of the substrate is close to the natural frequency of water ω_w (*i.e.,* when vibrational coupling is strong). We note that this frequency is related to the first zero-crossing time of velocity (momentum) autocorrelation of water, which is the boundary between the forward-scattering and the back-scattering (see supplementary Fig. 1 and 2 [38]). The natural frequency of water can be estimated as $\omega_w = \frac{1}{4\tau_1}$, where ω_w is the natural frequency of water and τ_1 is the first zero-crossing time of the velocity autocorrelation time. The

estimated natural frequency of bulk and interfacial water (*i.e.,* water in the contact layer) are 47 cm^{-1} and 52 cm^{-1}, respectively. As shown in the inset of Fig. 1(c), this frequency is the most dominant frequency of water, which corresponds to the intermolecular bending mode of water [39,40]. Fig. 1(d) shows the relation between contact angle and the total substrate-fluid adhesion energy, E_{sf}. The adhesion energy is considerably reduced (up to 76%) when $\omega_s \approx \omega_w$. The reduced adhesion energy results in an increased contact angle of water droplet. We will further discuss the mechanism of reduced adhesion energy in the later part of the manuscript. The results here imply that the wettability of a nanoscale system can be affected by the oscillation frequency of wall, which can be modified by experimental conditions and external means such as strain [41,42] and doping [41,43]. Also, the fact that interfacial vibrational coupling affects adsorption energy suggests that a solid-fluid interatomic force field considering interfacial vibrational coupling is necessary to study the interfacial phenomena more accurately.

To further understand how interfacial vibrational coupling reduces the wettability, we investigated the molecular structure and dynamics of the water droplet. Fig. 2(a) shows the interfacial structure of the water droplet for different frequencies of the substrate. The interfacial water layering is observed at the water-substrate interface, which is the result of the interplay between the solid-fluid interaction and the dynamics of water molecules. Noticeably, the interfacial water layering is substantially altered by interfacial vibrational coupling. The first peak of interfacial water structure is one of the factors that determines how strongly water and substrate interact. The stronger the liquid-solid adhesion, the higher the first peak. The strongest first peak is observed for the rigid membrane and the magnitude of the first peak decreases as ω_s approaches ω_w. This is in line with the computed contact angle as a lower first peak indicates a weaker water-substrate adhesion and thus a higher contact angle. Next, we investigated the dynamics of water

molecules in the contact layer. The contact layer is defined as the region between the substrate and the first valley of interfacial water layering (see Fig. 2(a)). We first calculated the residence time autocorrelation for the water molecules in the contact layer. The residence time autocorrelation function is given by $\zeta(t) \equiv \frac{\langle \beta(t+t_0)\beta(t_0) \rangle}{\langle \beta(t_0)\beta(t_0) \rangle}$, where t_0 is the reference time, t is the time elapsed from t_0, $\beta(t+t_0) = 1$ if the water molecule is continuously present in the contact layer between t_0 and $t + t_0$; otherwise $\beta(t + t_0) = 0$, and $\langle \cdots \rangle$ denotes the ensemble average. Physically, $\zeta(t)$ denotes the probability of residence of a water molecule in the contact layer over time. The decay of water-substrate correlation for different ω_s is plotted in Fig. 2(b). It shows that the interfacial vibrational coupling enhances the decay of residence time correlation, and this effect becomes more significant when ω_s approaches ω_w. The degree of residence time correlation decay can be quantified by the correlation time, $\tau_{CL} = \int_0^\infty \zeta(t)dt$. Physically, τ_{CL} is an indicator of the residence time of a water molecule in the contact layer. The residence time exhibits a minimum at a frequency around ω_w (see Supplementary Fig.3 [38]). To further understand how residence time is related to the contact angle, we visualized water molecules in the contact layer. Supplementary Fig.4 [38] shows that there are molecular-level void regions for both rigid and oscillating substrates that are created when water molecules leave the contact layer and are only occupied by other water molecules after a considerable amount of time. The presence of these void regions reduces the actual contact area. Furthermore, it is observed that these void regions appear more frequently for the oscillating case with a shorter residence time. Thus, a short residence time exhibits a smaller actual contact area and, as a result, has a smaller adhesion energy. The relation between substrate-fluid adhesion energy and the average time of contact is plotted in Fig. 2(c). It shows that a shorter contact time results in a smaller interaction energy between substrate and

water. Thus, a stronger interfacial vibrational coupling reduces the wettability. This mechanism of wetting reduction by reducing temporal contact resembles the well-explored mechanism of wetting reduction by reducing the spatial contact [10,44] in that the actual contact is reduced either temporally or spatially. Supplementary Fig. 2 [38] shows the strong ($\omega_s \approx \omega_w$) and weak vibrational coupling ($\omega_s \gg \omega_w$ or $\omega_s \ll \omega_w$). When the frequency of the substrate matches with the natural frequency of water, the momentum transfer is in-phase and reduces the temporal contact. One the other hand, the weak vibrational coupling results in a significant out-of-phase momentum transfer. To check any effects of temperature, we calculated the temperature of water droplet. Overall, the temperature of the droplet is maintained around the room temperature and only a slight rise of temperature (less than 4 K) is observed. As the contact angle is known to slightly decrease with increased temperature [45,46], temperature cannot be the reason for the dramatic increase of contact angle.

Next, we investigate how interfacial vibrational coupling effects water transport through a nanochannel constituting two graphene walls. We considered 4 nm thick water confined between two graphene walls oscillating with a certain frequency (see Fig. 3(a)). A constant force F is applied to the fluid molecules to generate flow (see the methods section for details). Fig. 3(b) shows the velocity profile and the density layering of water for different oscillation frequencies. Overall, the density layering, and the velocity of water are significantly affected by interfacial vibrational coupling. We observed plug-like velocity profiles for all the tested cases, which is observed in slip-dominant flow regime (*e.g.,* a low friction surface). Note that the slip velocity increases in the oscillating channels compared to that in the rigid channel. In the rigid channel, the water density near the channel wall is higher and the magnitude is reduced when the channel frequency matches with the natural frequency of water. This is consistent with the fact that solid-

fluid vibrational coupling weakens the solid-fluid interaction energy. The friction coefficient is given by the ratio between the frictional force per unit area and the slip velocity, $\lambda = \frac{\tau_s}{v_s}$, where τ_s is the shear stress exerted on the wall and v_s is the slip velocity [21]. It is confirmed that the applied forces are in the linear regime (the slip velocity and the driving forces) as shown in Fig. 3(c) regardless of the presence of interfacial vibrational coupling. Overall, the solid-fluid friction is reduced in the oscillating channel as shown in Fig. 3(d). The friction coefficient in the rigid graphene is 8.6 ± 1.7 kNsm^{-3}, which is close to the value 7.1 kNsm^{-3} we calculated using the Green-Kubo method [47]. The friction coefficient reduced up to 4.9 ± 0.8 kNsm^{-3} when ω_s is close to the natural frequency of confined water. This can also be understood as the reduced contact time at the strong vibrational coupling regime ($\omega_s \approx \omega_w$). Our finding shows that the fluid slip and wall-fluid friction coefficient can be modulated by the vibrational coupling at the solid-fluid interface.

We further investigated the interfacial vibrational coupling effect in water permeation through a nanoporous 2D membrane. In our previous study on water desalination using a 2D flexible membrane [48] we observed an enhanced water permeation in a flexible membrane compared to the rigid membrane. It was shown that the vibrational match between the membrane and water molecules increases the water permeation. In the present study, we considered pressure-driven water permeation through graphene nanopores of different diameters for various oscillating frequencies (see Fig. 4(a) and the Methods section for details). We note that the water permeation Q is in the linear regime for the various driving pressures considered regardless of the interfacial vibrational coupling (see Supplementary Fig. 5 [38]). Fig. 4(b) shows the velocity profiles of water in the nanopore. Similar to the flow in a nanochannel, interfacial vibrational coupling increases

slip velocity at the pore-water interface; however, the velocity profiles are not plug-like anymore. Fig. 4(c) highlights the interfacial vibrational coupling effects on the water permeation through the graphene nanopore. The enhancement in permeance is quantified by an enhancement factor, $\epsilon_Q = \frac{Q(\omega_s)}{Q_{Rigid}}$, where $Q(\omega_s)$ is the water permeance through an oscillating membrane with the frequency ω_s and Q_{Rigid} is the water permeance through the rigid membrane. The water permeation is enhanced near the most dominant frequency of water ω_w for all the tested pore sizes and the permeance when the frequency of membrane is higher or lower than the natural frequency of water (see the comparison of velocity profiles in high and low frequency regime in Supplementary Fig. 6 [38]). Note that the effect of interfacial vibrational coupling on the permeance is stronger in a smaller pore. Fig. 4(c) shows the permeation enhancement for various pore diameters. The maximum increase in permeation is 484% in the smallest nanopore, $D = 0.75$ nm. This implies that in this pore, the vibrational coupling can have a dominant role in transport phenomenon. Fig. 4(d) shows the enhancement factor for various pore diameters. This demonstrates that the interfacial vibrational coupling effect is increasingly important in a small pore and is negligible in a larger diameter pore ($\epsilon_Q < 1.01$ when $D > 40$ nm from data extrapolation shown in Fig. 4(d)). A similar trend was reported in water flow in mechanically actuated CNT [35] where the flow enhancement in small diameter CNT is higher compared to large diameter CNT. We observed two regimes of scaling between ϵ_Q and D. The nanopores smaller than 2.5 nm in diameter follow $\epsilon_Q \propto \frac{1}{\sqrt{D}}$, and the nanopores larger than 2.5 nm in diameter follow $\epsilon_Q \propto \frac{1}{D}$ as shown in the inset in Fig. 4(d). We attribute this to the overlap of the interfacial regions in smaller diameter pores. Based on the scaling and extrapolating the data for larger diameter pores, a less than 1% permeation

enhancement is expected for pores larger than 40 nm in diameter. On the other hand, up to 500%

enhancement is expected in sub-1nm pores.

CONCLUSION

The vibrational coupling at the solid-fluid interface plays an important role on wetting, fluid

slip, wall-fluid friction, and water transport. We observed that the contact angle changes with the

oscillation frequency of the substrate. The highest contact angle is observed when the vibrational

frequency of the substrate is close to the natural frequency of water corresponding to

intermolecular bending mode. We also observed a considerable reduction in solid-fluid adhesion

energy due to the strong solid-fluid vibrational coupling. To understand the mechanism

governing these observations, we studied the structure and dynamics of water near the interface.

Our statistical analysis of water-substrate correlation indicates that the interfacial vibrational

coupling reduces the time of contact between water and substrate, weakening the water-substrate

adhesion energy. The water slip in vibrating nanochannels is studied. We observed a higher slip

velocity and smaller friction coefficient when the vibration frequency of channel matches with

the natural frequency of water. The water transport through vibrating 2D nanopores shows

enhanced water transport due to the interfacial vibrational coupling and the enhancement factor

increases as the pore diameter decreases. Our results indicate that interfacial vibrational coupling

can considerably alter the physicochemical behavior of nanodevices depending on the frequency

regime. Furthermore, the modulation of interfacial vibrational coupling in mechanically excited

biological/synthetic nanochannel can be a novel way to achieve new functionality.

METHODS

Three different MD simulation setups were considered: 1) water droplet on graphene substrate, 2) water flow through a graphene channel (*i.e.,* water confined between two graphene channels), and 3) water permeation through a single layer of graphene nanopore. We considered atomically smooth graphene with rigid body motions prescribed by external vibrations for all the systems studied (*i.e.,* substrate, channel, and pore). The bond length between carbons of graphene was chosen as 0.1418 nm. The entire graphene substrate is harmonically oscillating in the out-of-plane direction with various frequencies ω_s keeping its average kinetic energy equal to the thermal energy $\frac{Nk_BT}{2}$, where N is the number of atoms, k_B is the Boltzmann constant and T is the temperature. We considered a fixed temperature of 298.15 K (*i.e.,* isothermal condition); thus, the vibrational energy is constant, and the amplitude decreases with increasing frequency. For all simulations, the SPC/E [49] water was used. The bond length and angle are kept constant using the SHAKE algorithm [50]. The van der Waals interactions are modeled using the LJ potential with a cut-off distance of 1.2 nm. The graphene-water potential parameters optimized by Wu and Aluru [36] are utilized. The PPPM method [51] was used to calculate the long-range Coulomb interactions with an accuracy of 10^{-5}. The temperature of water was maintained at 298.15 K using the Nosé-Hoover thermostat with a time constant 0.1 ps. The atomic trajectories were calculated in NVT ensemble with 1 fs time step. We utilized the Large-scale Atomic/Molecular Massively Parallel Simulator (LAMMPS) [52] for MD simulation and Open Visualization Tool (OVITO) [53] for visualization.

For the water contact angle simulation, 2014 water molecules, randomly generated in a 4.3 nm by 4.3 nm by 3.2 nm cubic box, were placed on top of a 10 nm by 10 nm single-layer graphene. The *z* dimension of the system (the direction perpendicular to the graphene surface) was set to be

8 nm and periodic boundary conditions were applied in all directions. MD simulations were performed for 5 ns for each case. The system was first equilibrated for 500 ps without oscillating the substrate and then, further equilibrated for 500 ps with a harmonic oscillation of the substrate. After the equilibration run, the data is obtained for 4 ns. During the post-processing of the density of the droplet, the center position of the droplet was calibrated every 10 ps.

For water flow in graphene confinement (water confined between two graphene channels), 2985 water molecules were placed between two graphene sheets spaced 4 nm apart in the x-direction. The y and z dimensions of graphene sheets were 5 nm. The periodic boundary condition was applied to the y and z coordinates and a fixed boundary condition was applied to the x coordinate. The electrostatic potential beyond the fixed boundary condition was turned off by putting an imaginary volume using slab option in PPPM solver. A constant force was applied to the oxygen atom of water in the z-direction (the armchair direction of graphene). The two graphene sheets oscillate in-phase in the x-direction with a frequency ω_s. The thermostat only controls the y-directional velocity component to minimize the disturbance to the water transport and interfacial vibrational coupling. Forces ranging from $F_0 = 0.02 \sim 0.08 \ \text{cal} \cdot \text{mol}^{-1}\text{Å}^{-1}$ were considered and linear flow is confirmed within the tested force range. For each vibrational frequency of graphene ω_s, 20 ns of simulations are performed. The first 2 ns data were discarded, and the rest of data are used to compute the velocity profile and density profile. The error in slip velocity was estimated as the standard deviation of slip velocities calculated every 2 ns.

For the water permeation through the graphene nanopore, three different sizes of pores were considered $D = 0.75, 2.75,$ and 4.04 nm. The x, y, and z dimensions of the system are 3.9 nm, 3.8 nm, and 12.0 nm for $D = 0.75$ nm pore; 5.9 nm, 5.9 nm, and 12.0 nm for $D = 2.75$ nm pore;

9.8 nm, 9.8 nm, and 12.0 nm for $D = 4.00$ nm pore. The graphene membrane is placed in the center of the z dimension of the system and solvated with water molecules. The graphene membrane oscillates with a frequency ω_s in the z-direction. To generate the hydrodynamic pressure, a constant z-directional force was applied to the oxygen atom in 1 nm thick box at each side of the system. When the simulation begins, the applied pressure gradually increases to the target pressure (25 ~ 200 Mpa) for 100 ps, and then maintained at the constant target pressure during the rest of the simulation. The data acquisition time depends on the size of the pore; 20 ns for $D = 0.75$ nm pore and 5 ns for $D = 2.75$ and 4.00 nm pores, and the first few hundred picosecond data were discarded. For the radial distribution of velocity, 0.34 nm high cylindrical bins were used.

AUTHOR INFORMATION

Corresponding Author

*E-mail: aluru@utexas.edu

Author Contributions

Y.N performed simulations, analysis, and wrote the manuscript under the guidance of N.A.

REFERENCES

[1] S. Bernèche and B. Roux, *Energetics of Ion Conduction through the K + Channel*, Nature **414**, 6859 (2001).

[2] T. W. Allen, O. S. Andersen, and B. Roux, *On the Importance of Atomic Fluctuations, Protein Flexibility, and Solvent in Ion Permeation*, Journal of General Physiology **124**, 679 (2004).

[3] M. Ma, F. Grey, L. Shen, M. Urbakh, S. Wu, J. Z. Liu, Y. Liu, and Q. Zheng, *Water Transport inside Carbon Nanotubes Mediated by Phonon-Induced Oscillating Friction*, Nature Nanotechnology **10**, 8 (2015).

[4] S. Marbach, D. S. Dean, and L. Bocquet, *Transport and Dispersion across Wiggling Nanopores*, Nature Physics **14**, 11 (2018).

[5] X. Zhang, Y. Guo, Z. Zhang, and P. Zhang, *Self-Cleaning Superhydrophobic Surface Based on Titanium Dioxide Nanowires Combined with Polydimethylsiloxane*, Applied Surface Science **284**, 319 (2013).

[6] L. Oberli, D. Caruso, C. Hall, M. Fabretto, P. J. Murphy, and D. Evans, *Condensation and Freezing of Droplets on Superhydrophobic Surfaces*, Advances in Colloid and Interface Science **210**, 47 (2014).

[7] M. Ferrari and A. Benedetti, *Superhydrophobic Surfaces for Applications in Seawater*, Advances in Colloid and Interface Science **222**, 291 (2015).

[8] W. Wang, Y. Lu, H. Zhu, and Z. Cao, *Superdurable Coating Fabricated from a Double-Sided Tape with Long Term "Zero" Bacterial Adhesion*, Advanced Materials **29**, 1606506 (2017).

[9] T. J. Hinton, A. Hudson, K. Pusch, A. Lee, and A. W. Feinberg, *3D Printing PDMS Elastomer in a Hydrophilic Support Bath via Freeform Reversible Embedding*, ACS Biomater. Sci. Eng. **2**, 1781 (2016).

[10] T.-S. Wong and C.-M. Ho, *Dependence of Macroscopic Wetting on Nanoscopic Surface Textures*, Langmuir **25**, 12851 (2009).

[11] C. T. Nguyen, M. Barisik, and B. Kim, *Wetting of Chemically Heterogeneous Striped Surfaces: Molecular Dynamics Simulations*, AIP Advances **8**, 065003 (2018).

[12] J. Rafiee, M. A. Rafiee, Z.-Z. Yu, and N. Koratkar, *Superhydrophobic to Superhydrophilic Wetting Control in Graphene Films*, Advanced Materials **22**, 2151 (2010).

[13] C. D. Daub, D. Bratko, K. Leung, and A. Luzar, *Electrowetting at the Nanoscale*, J. Phys. Chem. C **111**, 505 (2007).

[14] B. Shi and V. K. Dhir, *Molecular Dynamics Simulation of the Contact Angle of Liquids on Solid Surfaces*, J. Chem. Phys. **130**, 034705 (2009).

[15] T. Li, J. Li, H. Lin, Y. Duan, Y. Xia, Y. Jiang, and H. Li, *Control of Wettability Transition and Coalescence Dynamics of Droplets on the Surface via Mechanical Vibration: A Molecular Simulation Exploration*, Applied Surface Science **473**, 393 (2019).

[16] T. Werder, J. H. Walther, R. L. Jaffe, T. Halicioglu, and P. Koumoutsakos, *On the Water−Carbon Interaction for Use in Molecular Dynamics Simulations of Graphite and Carbon Nanotubes*, J. Phys. Chem. B **107**, 1345 (2003).

[17] M. Barisik and A. Beskok, *Wetting Characterisation of Silicon (1,0,0) Surface*, Molecular Simulation **39**, 700 (2013).

[18] M. Majumder, N. Chopra, R. Andrews, and B. J. Hinds, *Enhanced Flow in Carbon Nanotubes*, Nature **438**, 44 (2005).

[19] J. K. Holt, H. G. Park, Y. Wang, M. Stadermann, A. B. Artyukhin, C. P. Grigoropoulos, A. Noy, and O. Bakajin, *Fast Mass Transport Through Sub-2-Nanometer Carbon Nanotubes*, Science **312**, 1034 (2006).

[20] Q. Xie, M. A. Alibakhshi, S. Jiao, Z. Xu, M. Hempel, J. Kong, H. G. Park, and C. Duan, *Fast Water Transport in Graphene Nanofluidic Channels*, Nature Nanotech **13**, 238 (2018).

[21] K. Falk, F. Sedlmeier, L. Joly, R. R. Netz, and L. Bocquet, *Molecular Origin of Fast Water Transport in Carbon Nanotube Membranes: Superlubricity versus Curvature Dependent Friction*, Nano Lett. **10**, 4067 (2010).

[22] N. Wei, X. Peng, and Z. Xu, *Breakdown of Fast Water Transport in Graphene Oxides*, Phys. Rev. E **89**, 012113 (2014).

[23] S. Joseph and N. R. Aluru, *Why Are Carbon Nanotubes Fast Transporters of Water?*, Nano Lett. **8**, 452 (2008).

[24] Y. Zhu and S. Granick, *Limits of the Hydrodynamic No-Slip Boundary Condition*, Phys. Rev. Lett. **88**, 106102 (2002).

[25] O. I. Vinogradova and A. V. Belyaev, *Wetting, Roughness and Flow Boundary Conditions*, J. Phys.: Condens. Matter **23**, 184104 (2011).

[26] C. Cottin-Bizonne, J.-L. Barrat, L. Bocquet, and E. Charlaix, *Low-Friction Flows of Liquid at Nanopatterned Interfaces*, Nature Mater **2**, 237 (2003).

[27] E. Bonaccurso, H.-J. Butt, and V. S. J. Craig, *Surface Roughness and Hydrodynamic Boundary Slip of a Newtonian Fluid in a Completely Wetting System*, Phys. Rev. Lett. **90**, 144501 (2003).

[28] M. Heiranian and N. R. Aluru, *Nanofluidic Transport Theory with Enhancement Factors Approaching One*, ACS Nano **14**, 272 (2020).

[29] P. A. Thompson and S. M. Troian, *A General Boundary Condition for Liquid Flow at Solid Surfaces*, Nature **389**, 360 (1997).

[30] J. P. Rothstein, *Slip on Superhydrophobic Surfaces*, Annual Review of Fluid Mechanics **42**, 89 (2010).

[31] D. M. Huang, C. Sendner, D. Horinek, R. R. Netz, and L. Bocquet, *Water Slippage versus Contact Angle: A Quasiuniversal Relationship*, Phys. Rev. Lett. **101**, 226101 (2008).

[32] K. Huang and I. Szlufarska, *Friction and Slip at the Solid/Liquid Interface in Vibrational Systems*, Langmuir **28**, 17302 (2012).

[33] A. Sam, S. K. Kannam, R. Hartkamp, and S. P. Sathian, *Water Flow in Carbon Nanotubes: The Effect of Tube Flexibility and Thermostat*, J. Chem. Phys. **146**, 234701 (2017).

[34] A. T. Celebi, C. T. Nguyen, R. Hartkamp, and A. Beskok, *The Role of Water Models on the Prediction of Slip Length of Water in Graphene Nanochannels*, J. Chem. Phys. **151**, 174705 (2019).

[35] W. Cao, J. Wang, and M. Ma, *Mechano-Nanofluidics: Water Transport through CNTs by Mechanical Actuation*, Microfluid Nanofluid **22**, 125 (2018).

[36] Y. Wu and N. R. Aluru, *Graphitic Carbon–Water Nonbonded Interaction Parameters*, J. Phys. Chem. B **117**, 8802 (2013).

[37] C. T. Nguyen and B. Kim, *Stress and Surface Tension Analyses of Water on Graphene-Coated Copper Surfaces*, Int. J. Precis. Eng. Manuf. **17**, 503 (2016).

[38] See Supplemental Material at URL for additional data on velocity autocorrelation function and vibrational coupling, residence time with respect to frequency, molecular-level void

regions in contact Layer, a linear water flux over the pressure, and velocity profiles for various frequencies.

[39] G. E. Walrafen, Y. C. Chu, and G. J. Piermarini, *Low-Frequency Raman Scattering from Water at High Pressures and High Temperatures*, J. Phys. Chem. **100**, 10363 (1996).

[40] R. A. X. Persson, V. Pattni, A. Singh, S. M. Kast, and M. Heyden, *Signatures of Solvation Thermodynamics in Spectra of Intermolecular Vibrations*, J. Chem. Theory Comput. **13**, 4467 (2017).

[41] G. Kukucska and J. Koltai, *Theoretical Investigation of Strain and Doping on the Raman Spectra of Monolayer MoS2*, Physica Status Solidi (b) **254**, 1700184 (2017).

[42] Y. Wang, C. Cong, C. Qiu, and T. Yu, *Raman Spectroscopy Study of Lattice Vibration and Crystallographic Orientation of Monolayer MoS2 under Uniaxial Strain*, Small **9**, 2857 (2013).

[43] S. K. Saha, R. Ch. Chandrakanth, H. R. Krishnamurthy, and U. V. Waghmare, *Mechanisms of Molecular Doping of Graphene: A First-Principles Study*, Phys. Rev. B **80**, 155414 (2009).

[44] A. B. D. Cassie and S. Baxter, *Wettability of Porous Surfaces*, Trans. Faraday Soc. **40**, 546 (1944).

[45] F. Taherian, V. Marcon, N. F. A. van der Vegt, and F. Leroy, *What Is the Contact Angle of Water on Graphene?*, Langmuir **29**, 1457 (2013).

[46] J. D. Bernardin, I. Mudawar, C. B. Walsh, and E. I. Franses, *Contact Angle Temperature Dependence for Water Droplets on Practical Aluminum Surfaces*, International Journal of Heat and Mass Transfer **40**, 1017 (1997).

[47] L. Bocquet and J.-L. Barrat, *On the Green-Kubo Relationship for the Liquid-Solid Friction Coefficient*, J. Chem. Phys. **139**, 044704 (2013).

[48] Y. Noh and N. R. Aluru, *Phonon-Fluid Coupling Enhanced Water Desalination in Flexible Two-Dimensional Porous Membranes*, Nano Lett. **22**, 419 (2022).

[49] H. J. C. BERENDSEN, J. R. GRIGERA, and T. P. STRAATSMA, *The Missing Term in Effective Pair Potentials*, J. Phys. Chem. (1952) **91**, 6269 (1987).

[50] J.-P. Ryckaert, G. Ciccotti, and H. J. C. Berendsen, *Numerical Integration of the Cartesian Equations of Motion of a System with Constraints: Molecular Dynamics of n-Alkanes*, Journal of Computational Physics **23**, 327 (1977).

[51] R. W. Hockney and J. W. Eastwood, *Computer Simulation Using Particles*, Computer Simulation Using Particles, New York: McGraw-Hill, 1981 (1981).

[52] S. Plimpton, *Fast Parallel Algorithms for Short-Range Molecular Dynamics*, Journal of Computational Physics **117**, 1 (1995).

[53] A. Stukowski, *Visualization and Analysis of Atomistic Simulation Data with OVITO–the Open Visualization Tool*, Modelling and Simulation in Materials Science and Engineering **18**, 015012 (2010).
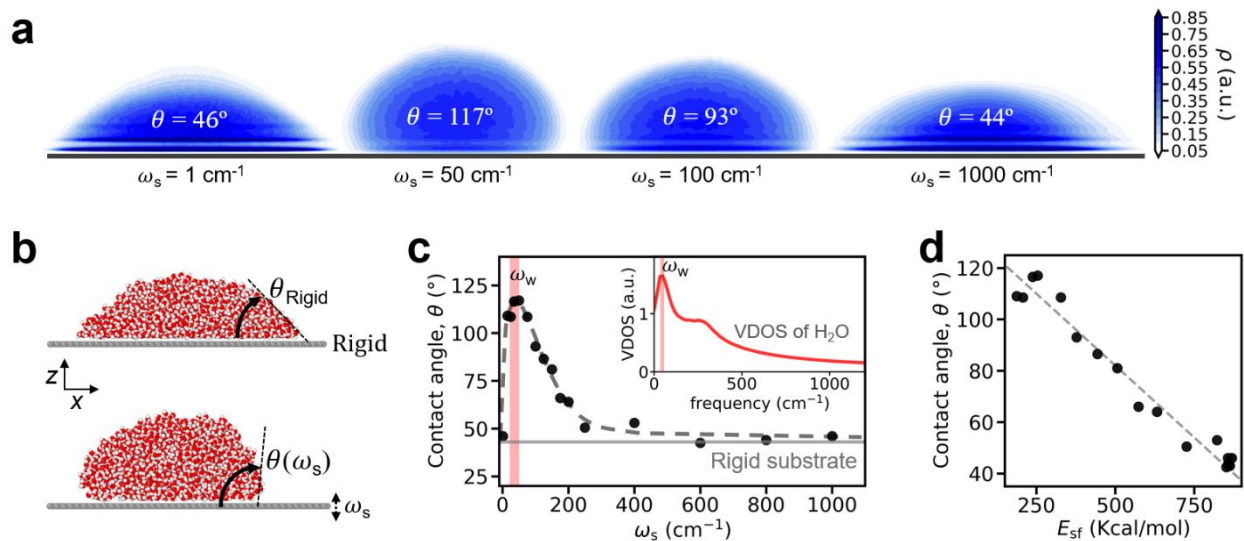
FIG. 1. Interfacial vibrational coupling induced wettability change. (a) Water droplets on substrates with different oscillation frequencies visualized by the density. (b) MD snapshots for water droplet on a rigid substrate (top) and on an oscillating substrate (bottom). (c) Contact angle as a function of frequency of the substrate. The black dots are MD data, and the gray dashed line is a fit to the MD data. The inset shows the VDOS of water molecule. The red shaded area represents the natural frequency of water ω_{w}. The gray solid line is the contact angle on a rigid substrate. (d) The relation between the contact angle and the total adhesion energy between the substrate and fluid, E_{sf}. The gray dashed line is a linear fitting.
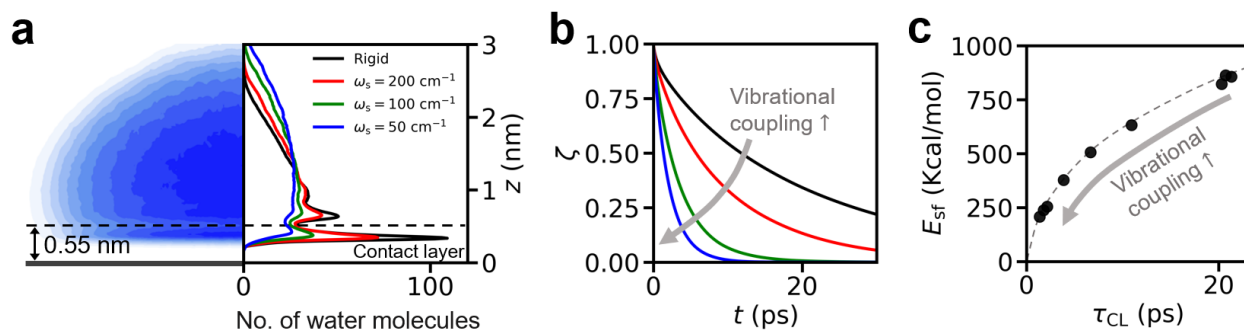
20

FIG. 2. Mechanism governing wettability change due to interfacial vibrational coupling. (a) Interfacial structures of water droplet on a graphene substrate for various vibrational frequencies. The contact layer is defined as the region between graphene and the first valley of the interfacial layering of water molecules. (b) Decay of residence time autocorrelation of water in the contact layer for various frequencies of the substrate (see the legend in Fig 2(a)). (c) Total attraction energy between water and substrate and the average time of contact. The dots are MD simulations and the dashed line is a fit to the data.
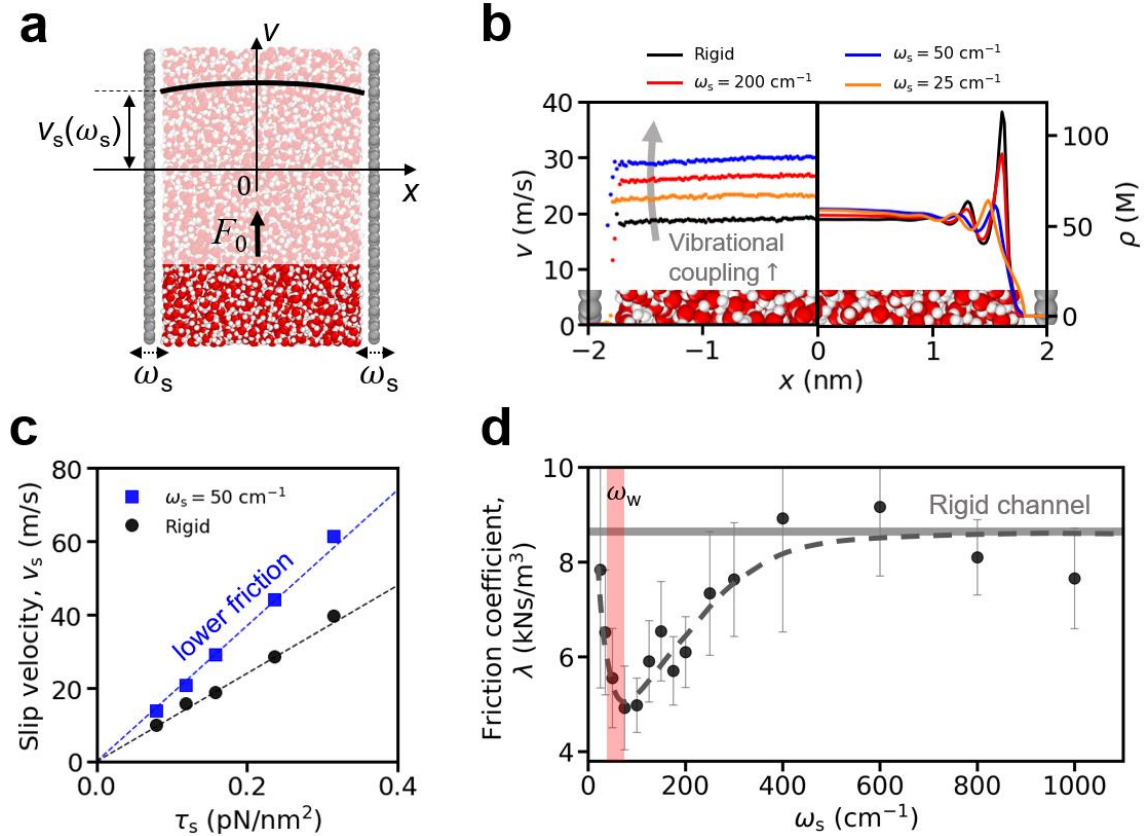
FIG. 3. Effects of interfacial vibrational coupling on slip and friction. (a) Schematic of MD simulation for water transport in graphene confinement. (b) Velocity profile (left) and the interfacial structure of water (right) for different frequencies of channel wall for $F_0 = 0.04$ cal · mol^{-1}Å^{-1}. (c) Linear relation between the slip velocity and shear stress exerted on the wall by the fluid. The dashed lines are linear fits. (d) Reduced friction due to the interfacial vibrational coupling. The black dots are MD data, and the gray dashed line is a fit to the data. The error bars are the standard deviation of friction coefficients for several sets of 2 ns trajectories. The gray solid line represents the friction coefficient of rigid channel. The red shaded area indicates the natural frequency of water.
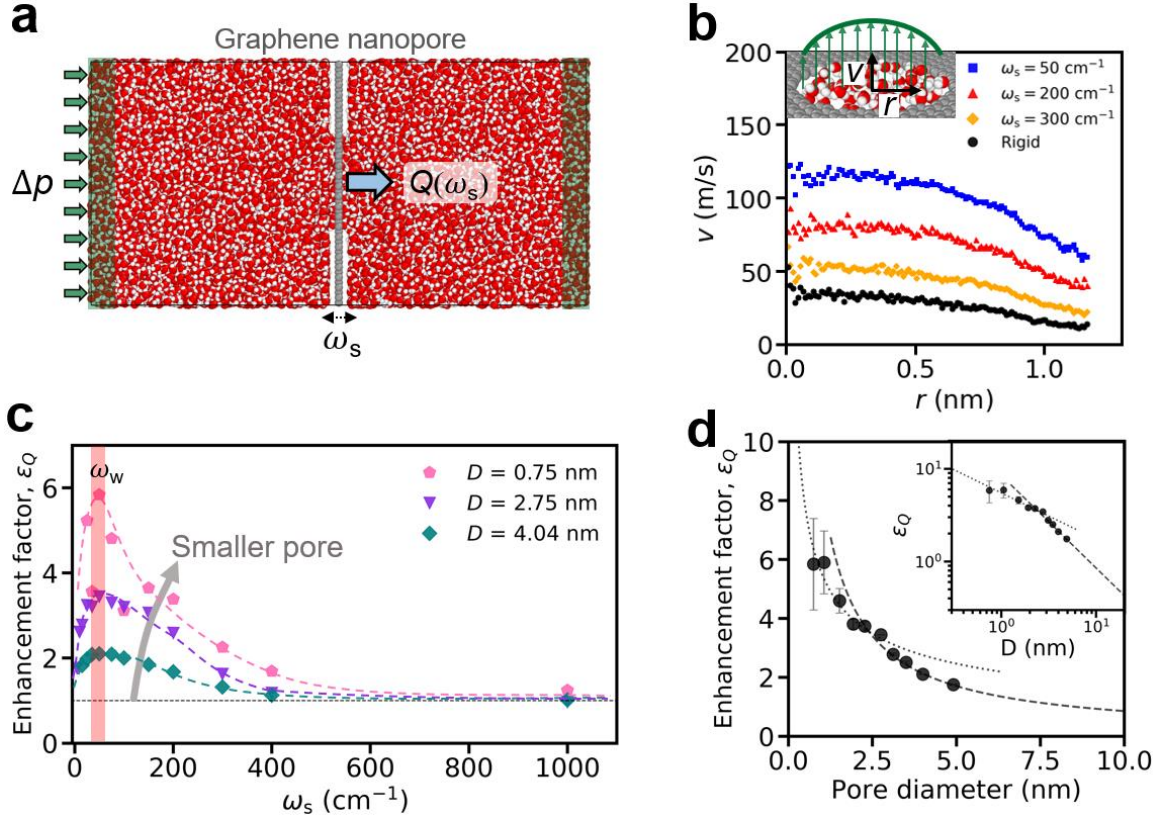
FIG. 4. Interfacial vibrational coupling enhanced water permeation through graphene nanopores. (a) Schematic of MD simulation for water permeation driven by a pressure gradient. (b) Enhanced water velocity in the nanopore due to interfacial vibrational coupling (see the legend in Fig 4(c)) for $D = 2.75$ nm and $\Delta p = 100$ Mpa. (c) Enhancement of permeance as a function of oscillation frequency for three different diameter pores. The red shaded area indicates the natural frequency of water. The dashed lines are fits to the data. (d) The enhancement in permeance for various size nanopores at $\omega_s = 50$ cm^{-1} and $\Delta p = 100$ Mpa. The inset shows the log scale plot. The dashed line and dotted line are the fitted curve with $\epsilon_Q \propto \frac{1}{D}$ and $\epsilon_Q \propto \frac{1}{\sqrt{D}}$, respectively.